

Heteronuclear long-range Rydberg molecules

Michael Peper¹ and Johannes Deiglmayr^{1,2}

¹Laboratory of Physical Chemistry, ETH Zürich, 8093 Zürich, Switzerland

²Department of Physics and Geoscience, University of Leipzig, 04109 Leipzig, Germany*

(Dated: June 6, 2022)

We present the formation of homonuclear Cs_2 , K_2 , and heteronuclear CsK long-range Rydberg molecules in a dual-species magneto-optical trap for ^{39}K and ^{133}Cs by one-photon UV photoassociation. The different ground-state-density dependence of homo- and heteronuclear photoassociation rates and the detection of stable molecular ions resulting from auto-ionization provide an unambiguous assignment. We perform bound-bound millimeter-wave spectroscopy of long-range Rydberg molecules to access molecular states not accessible by one-photon photoassociation. A comparison to binding energies calculated with the most recent theoretical model and atomic parameters reveals the inadequacy of this approach to correctly describe the full set of our observations from homo- and heteronuclear long-range Rydberg molecules. We show that the data from photoassociation spectroscopy of heteronuclear long-range Rydberg molecules provides a benchmark for the development of theoretical models which facilitate the accurate extraction of low-energy electron-neutral scattering phase shifts.

Long-range Rydberg molecules (LRMs) are bound states of a Rydberg atom and a ground-state atom located within the orbit of the Rydberg electron [1, 2]. The binding results from the scattering of the almost free Rydberg electron off the ground-state atom, which was first described by Fermi [3]. For low-energy collisions, the interaction strength is proportional to the probability density of the Rydberg electron's wavefunction and the S -wave scattering length. For negative scattering lengths and Rydberg atoms in states with high principal quantum number n , the oscillatory interaction potential supports bound states at internuclear separations $R \sim 2a_0 n^2$ close to the classical turning point of the Rydberg electron [4]. Homonuclear LRMs were first observed by photoassociation in rubidium [5], followed by observations in cesium, rubidium, and strontium [6–11]. Given an accurate theoretical model to describe their binding, LRMs can yield precise data on low-energy electron-neutral collisions ($E_{\text{col}} \leq 100$ meV) [10, 12, 13] which is not accessible otherwise and is of greatest relevance in many fields including low temperature plasmas, radiation chemistry and biology [14].

In this letter we show that heteronuclear LRMs provide a stringent test for current theoretical models because the contributions from Rydberg atom and perturber can be varied separately, similarly to the established methods of isotopic and isoelectronic substitution in chemistry [15]. By photoassociation below $n^2\text{P}_{3/2}$ Rydberg states in a dual-species magneto-optical trap (dsMOT) of ^{133}Cs and ^{39}K we create homonuclear Cs_2 and K_2 LRMs as well as heteronuclear LRMs. Millimeter-wave spectroscopy of CsK LRMs yields additional data on $n^2\text{S}_{1/2}$ Rydberg states. A comparison to theoretical calculations reveals the inadequacy of current theoretical tools to correctly describe the full set of our observations for homo- and heteronuclear LRMs.

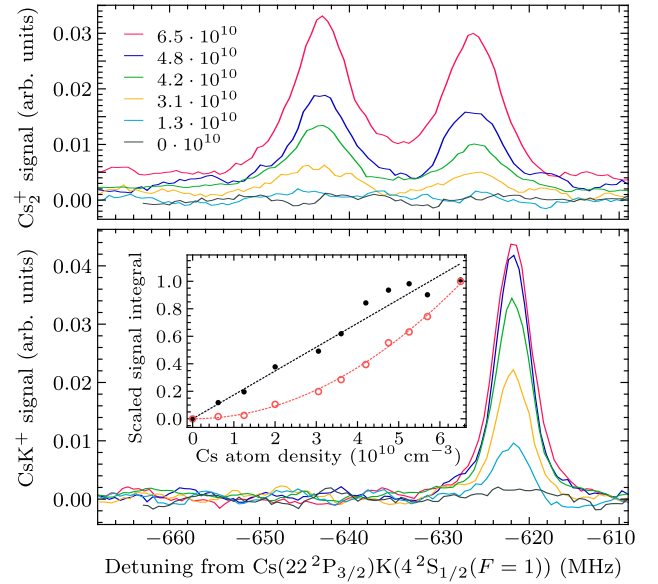


Figure 1. (upper panel) Cs_2^+ and (lower panel) CsK^+ ion signals as a function of the photoassociation laser detuning from the $\text{Cs}(22^2\text{P}_{3/2})\leftarrow\text{Cs}(6^2\text{S}_{1/2}(F=3))$ transition recorded after $25\mu\text{s}$ of PA. The Cs density was varied (legend in upper panel, values in cm^{-3}) and the K density was $2.5(3) \cdot 10^{10} \text{ cm}^{-3}$. (inset) Full (open) circles are the scaled integrals of the CsK^+ (Cs_2^+) signal. Dashed lines represent linear and quadratic fits.

A dual-species MOT (dsMOT) is formed by two background-vapour-loaded MOTs for ^{133}Cs and ^{39}K , spatially overlapped in an ultra-high vacuum chamber featuring electrodes for precise electric-field control and a micro-channel plate detector [16, 17]. The two atomic clouds are overlapped by coupling all laser beams for the two MOTs out of common single-mode fibers. The overlap is monitored by absorption images and is optimized by small changes to the alignment of the trapping beams and their intensities. Typical values for atom num-

* johannes.deiglmayr@uni-leipzig.de

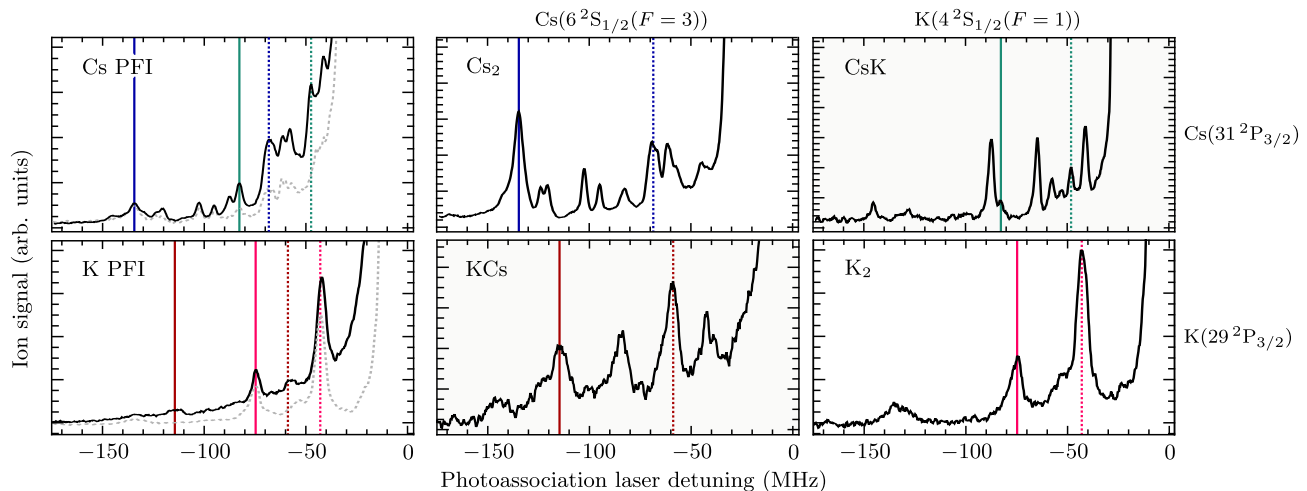


Figure 2. Photoassociation spectra of Cs (K) atoms prepared in the $F = 3$ ($F = 1$) ground state. (upper row) Cs PFI (left), Cs_2^+ (middle), and CsK^+ (right) autoionization signal recorded below the $\text{Cs}(31^2\text{P}_{3/2}) \leftarrow \text{Cs}(6^2\text{S}_{1/2}(F = 3))$ transition. Resonances assigned to the $v = 0$ level in the outermost well of the $^3\Sigma^+$ ($^1,^3\Sigma^+$) states are marked by full (dotted) blue (Cs_2) and green (CsK) lines. (bottom row) K PFI (left), KCs^+ (middle), and K_2^+ (right) autoionization signal below the $\text{K}(29^2\text{P}_{3/2}) \leftarrow \text{K}(4^2\text{S}_{1/2}(F = 1))$ transition. Resonances assigned to the $v = 0$ level in the outermost well of the $^3\Sigma^+$ ($^1,^3\Sigma^+$) states are marked by full (dotted) magenta (K_2) and red (KCs) lines. The autoionization and PFI signals (gray dotted line in left panels) for Cs_2 and K_2 were recorded in single-species MOTs.

ber, peak density, and temperature are $8 \cdot 10^6$ ($5 \cdot 10^6$), $2 \cdot 10^{10} \text{ cm}^{-3}$ ($4 \cdot 10^{10} \text{ cm}^{-3}$) and $40 \mu\text{K}$ ($20 \mu\text{K}$) for the cesium (potassium) MOT. LRMs are formed by one-photon photoassociation using UV-laser pulses of $10 \mu\text{s}$ to $30 \mu\text{s}$ length and a peak intensity of 200 W cm^{-2} . The UV radiation is obtained by frequency-doubling the output of a continuous-wave (cw) ring dye laser at 639 nm (571 nm) for Rydberg states of cesium (potassium). Its frequency is measured by a wavemeter (HighFinesse WS7), calibrated to the D2 line of potassium every few seconds. Measurements with an optical frequency comb [16] showed that this calibration procedure yields errors below 1.5 MHz in the UV for frequency shifts of up to 200 MHz . Following photoassociation, a ramped electric field is applied to state- and mass-selectively detect products [10]. The ionization field of an LRM is similar to the one of the corresponding atom, which facilitates bound-bound spectroscopy by millimeter waves [17].

When photoassociation is performed in a mixture of species A and B, both homonuclear and heteronuclear molecules may be created. Pulsed-field ionization (PFI) does not allow us to distinguish between A_2 and AB , because the molecule dissociates instantaneously upon removal of the Rydberg electron and in both cases A^+ is detected. However, AB (A_2) may autoionize to form a stable molecular ion AB^+ (A_2^+) [18, 19]. A photoassociated molecule is thus detected either as atomic or molecular ion, depending on the autoionization rate which may vary strongly for different molecular states. We use the labels KCs (CsK) to distinguish between heteronuclear LRMs where potassium (cesium) is in a Rydberg state, although these are chemically identical species. Fig. 1 shows the Cs_2^+ and CsK^+ signals when the frequency of

the photoassociation laser applied to the dsMOT is tuned below the $\text{Cs}(22^2\text{P}_{3/2}) \leftarrow \text{Cs}(6^2\text{S}_{1/2}(F = 3))$ transition. Clear resonances appear when the density of Cs ground-state atoms is increased. The detection of CsK^+ ions constitutes an unambiguous signature for the formation of heteronuclear LRMs. The number of heteronuclear ions depends linearly on the density of Cs ground-state atoms while the number of Cs_2^+ ions exhibits a quadratic dependence, as expected for non-saturated photoassociation (see Appendix A) [20].

Photoassociation spectra below the $\text{Cs}(31^2\text{P}_{3/2})$ asymptote (upper row) and below the $\text{K}(29^2\text{P}_{3/2})$ asymptote (lower row) are shown in Fig. 2. The effective quantum numbers $n^* = n - \delta$, where δ is the quantum defect, of the two states are 27.44 [16] and 27.29 [17], respectively, and the properties of the Rydberg electron are almost identical. The PFI signal obtained in the dsMOT (left panel, black line) exhibits dense series of resonances above -150 MHz , resulting from photoassociation of LRMs. The detuning of a resonance from the atomic Rydberg transition directly yields its binding energy. At detunings above approx. -30 MHz , the molecular resonances are masked by off-resonant excitation of Rydberg atoms and Rydberg-atom pairs [18]. For comparison, photoassociation spectra obtained in the single-species MOTs (gray-dashed lines) are shown. Photoassociation in the dsMOT yields overall larger signals, but only few additional resonances can be identified unambiguously. The signals of molecular ions resulting from autoionization are shown in the central and right-hand panels and allow us to assign resonances in the PFI spectra to homo- or heteronuclear LRMs. As an example, the position of the strong resonance in the Cs PFI spec-

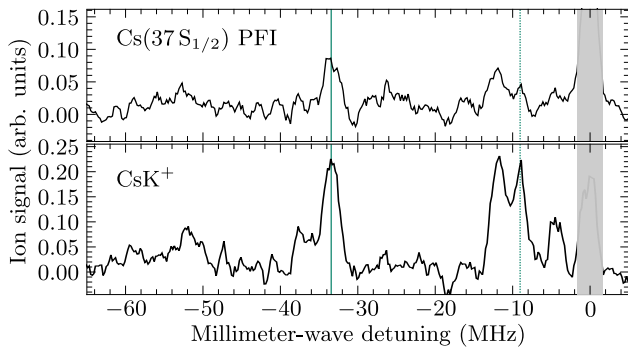


Figure 3. (upper panel) $\text{Cs}(37S_{1/2})$ PFI and (lower panel) CsK^+ signal as function of the millimeter-wave detuning from the $\text{Cs}(37^2S_{1/2}) \leftarrow \text{Cs}(37^2P_{3/2})\text{K}(4^2S_{1/2}(F=2))(^3\Sigma^+(v=0))$ transition. The resonance assigned to the $v=0$ level in the outermost well of the $^3\Sigma^+$ ($^{1,3}\Sigma^+$) state is marked by a full (dotted) green line. The gray bar masks a spurious signal from two-photon excitation of atomic Rydberg states caused by overlapping UV and millimeter-wave pulses.

tra at -83 MHz is marked in the upper panels by a green line. This resonance is assigned to CsK based on the observations that (i) its intensity is much stronger when photoassociation occurs in the dsMOT and (ii) it is also present in the CsK^+ signal. Because of the dense spectra of homo- and heteronuclear LRMs when Cs is excited, many of their photoassociation resonances overlap. The photon energy required to excite K atoms into Rydberg states is sufficient to ionize Cs ground-state atoms. Because the cross section for this process is small, we observe only few Cs^+ ions when exciting K in the dsMOT, which might cause a broadening of the spectra in panels “K PFI” and “KCs”.

Millimeter-wave spectroscopy of LRMs allows us to probe molecular states correlating to Rydberg states with different angular momenta. Fig. 3 shows exemplary millimeter-wave spectra of CsK molecules formed by photoassociation in the $v=0$ level of the $^3\Sigma^+$ state correlated to the $\text{Cs}(37^2P_{3/2})\text{K}(4^2S_{1/2}(F=2))$ asymptote, where transitions to $\text{Cs}(37^2S_{1/2})\text{K}(4^2S_{1/2}(F=2))$ molecular states are driven by a $10\text{ }\mu\text{s}$ millimeter-wave pulse following PA (see Appendix F). Because of the almost integer quantum defect of cesium $n^2S_{1/2}$ states ($\delta = 4.04$), these states lie just below the degenerate manifold of high- l Rydberg states and are strongly influenced by LRMs correlated to these asymptotes [4, 21–23]. The autoionization signal (lower panel) exhibits several resonances originating from transitions to states with higher autoionization rates. These resonances also appear in the PFI signal for $\text{Cs}(37^2S_{1/2})$ Rydberg states (upper panel), which confirms millimeter-wave-induced population transfer.

To assign observed resonances, we calculate the potential energy curves (PEC) for homo- and heteronuclear LRMs using the Hamiltonian given by Eiles and Greene [24] and the most recent theoretical phase shifts [25, 26]. The phase shifts depend on the collision energy, which is

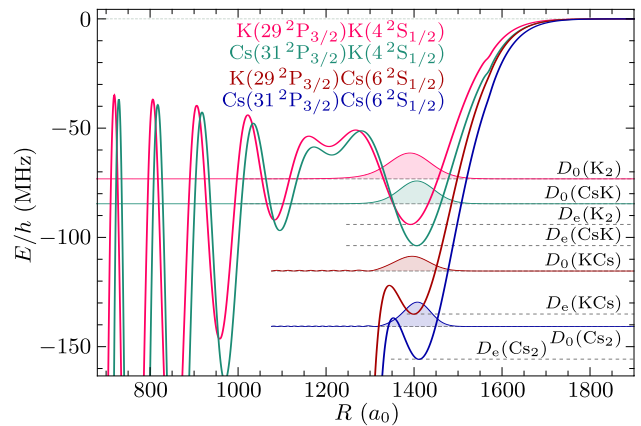


Figure 4. $^3\Sigma^+(\Omega=1/2)$ interaction potentials correlating to the indicated molecular asymptotes. The minima of the outermost potential well D_e are marked by dashed gray lines. The energy D_0 of the vibrational ground states and the respective probability densities are indicated by filled curves.

taken as the semi-classical kinetic energy of the Rydberg electron

$$E_{\text{col}} = \frac{2}{R} - \frac{1}{n_{\text{ref}}^2} \quad (1)$$

in the potential of the Rydberg-atom core. The hydrogenic manifold above the state of interest ($n=28$ for the n^2P states studied here) is chosen as reference n_{ref} [24, 25].

The Hamiltonian is evaluated in an atomic product basis, consisting of the nuclear and electronic spins (i, m_i, s, m_s) of the ground-state atom and a set of states (n, l, j, m_j) of the Rydberg atom, where m_i , m_s , and m_j are the projections of i , s , and j on the internuclear axis. The projection of the total angular momentum excluding rotation on the internuclear axis, $\Omega = m_i + m_s + m_j$, is a conserved quantity and we perform the calculation separately for each Ω . The choice of the basis set is ambiguous, because the eigenenergies do not converge when more states are included [27]. We optimize the basis size separately for each perturber to reproduce the experimental data. The electronic states obtained in our calculations are labeled by the dominant projection of the orbital angular momentum on the internuclear axis, $\Lambda = m_l$, and the spin-character of contributing scattering channels. $^3\Lambda$ states have only binding contributions from scattering channels with a total electronic spin $S=1$, while $^{1,3}\Lambda$ states are of mixed $S=0$ and $S=1$ character and have smaller, F -dependent binding energies [8].

In Fig. 4, the calculated PECs of $^3\Sigma^+(\Omega=1/2)$ states are drawn for Cs_2 , K_2 , KCs and CsK . Molecular states below the $\text{Cs}(31^2P_{3/2})\text{Cs}(6^2S_{1/2})$ and $\text{K}(29^2P_{3/2})\text{Cs}(6^2S_{1/2})$ asymptotes are strongly perturbed by the 3P_0 shape resonance of the electron-cesium scattering, which causes the steep drop of the PEC at about $R \approx 1300 a_0$ [26]. The fine-structure splitting of this 3P_J resonance lifts the degeneracy of the PECs for

Table I. Calculated dissociation energies D_e , and calculated (D_0) and experimental ($D_{0,\text{exp}}$) binding energies of the $v = 0$ level of the outermost well. The experimental uncertainty is estimated from the calibration uncertainty (see text) and the linewidth. The last column contains the deviation of the experimental binding energies relative to the calculated ones.

Asymptote	State	D_e/h (MHz)	D_0/h (MHz)	$D_{0,\text{exp}}/h$ (MHz)	
Cs($31^2P_{3/2}$)Cs($6^2S_{1/2}(F=3)$)	$^3\Sigma^+$	-155.5	-140.2	-134.3(15)	-4.2 %
	$^{1,3}\Sigma^+$	-78.2	-67.6	-68.6(15)	+1.5 %
K($29^2P_{3/2}$)Cs($6^2S_{1/2}(F=3)$)	$^3\Sigma^+$	-134.7	-114.7	-114.3(20)	-0.3 %
	$^{1,3}\Sigma^+$	-73.0	-61.7	-59.6(20)	-3.4 %
K($29^2P_{3/2}$)K($4^2S_{1/2}(F=1)$)	$^3\Sigma^+$	-94.0	-73.2	-74.5(20)	+1.1 %
	$^{1,3}\Sigma^+$	-50.3	-37.9	-42.1(20)	+11.3 %
Cs($31^2P_{3/2}$)K($4^2S_{1/2}(F=1)$)	$^3\Sigma^+$	-103.7	-84.6	-82.7(15)	-2.2 %
	$^{1,3}\Sigma^+$	-60.2	-46.9	-47.8(15)	+1.9 %
Cs($37^2S_{1/2}$)K($4^2S_{1/2}(F=2)$)	$^3\Sigma$	-70.2	-50.4	-33.4(5)	-33.7 %
	$^{1,3}\Sigma$	-26.2	-15.6	-9.1(5)	-41.7 %

different values of Ω [28]. However, except for the largest value $\Omega = 7/2$, the values for D_e are within 2 MHz and we report their mean value (see Appendix C). Dissociation energies D_e of the outermost well of the PECs are summarized in Table I. The PECs of homo- and heteronuclear molecules with the same perturber are similar, because phase shifts and hyperfine interaction of the ground-state atom are the same. The difference between CsK and K₂ (KCs and Cs₂) originates mostly in the different spin-orbit couplings of the Rydberg states, and in the different effective quantum numbers. The dissociation energy for the Cs($31^2P_{3/2}$)Cs($6^2S_{1/2}$) PEC is about 50 % larger than for the Cs($31^2P_{3/2}$)K($4^2S_{1/2}$) PEC, close to the ratio of zero-energy triplet scattering lengths of ^{39}K and cesium [25]. Previous studies have shown that the vibrational $v = 0$ levels in the outermost wells of the $^3\Sigma^+$ and $^{1,3}\Sigma^+$ PECs are always observed as strong resonances in photoassociation spectra [10] and we thus focus on these levels. Binding energies and vibrational wavefunctions (see Fig. 4) are determined by the modified Milne phase-amplitude method [29] (see Appendix D) and reported in Table I. We neglect the rotation of the LRMs, because our spectra do not resolve rotational states. The PEC of the $^3\Sigma^+$ state of Cs₂ supports a single vibrational level. In KCs, this level becomes a resonance bound by quantum scattering at the steep drop of the PEC [30]. The calculated width of this resonance is $\Gamma_{\text{FWHM}} = 7.9 \text{ MHz}$, in agreement with the observed width of 7.7(7) MHz.

We assign experimental resonances following three criteria: (i) a strong PFI signal, (ii) agreement with calculated binding energies, and (iii) a comparison between spectra recorded with atoms prepared in different hyperfine states ($^3\Sigma^+$ resonances do not depend on F [8, 10]) (see Appendix E). The resulting assignment is indicated in Fig. 2. For the states where Cs is the perturber (Cs₂ and KCs), we find the best agree-

ment (*i.e.*, the smallest root mean squared deviation $\sigma_{\text{rms}} = 3.2 \text{ MHz}$) for a basis set including manifolds $n = 27 - 28$. The calculated and observed line positions agree within the experimental uncertainty, except for the $^3\Sigma^+$ resonance of Cs₂, where the calculation overestimates the binding energy by four times the experimental uncertainty. However, the experimental assignment of this resonance is unambiguous and the discrepancy increases when increasing the basis set. For nP states where K is the perturber, we find the best agreement $\sigma_{\text{rms}} = 2.4 \text{ MHz}$ for a basis including manifolds $n = 27 - 30$, with a significant deviation for the K₂ $^{1,3}\Sigma^+$ resonance. Using the analogous basis set $n = 32 - 35$ (one asymptote below, three above the state of interest) for Cs($37^2S_{1/2}$)K($4^2S_{1/2}$) overestimates D_0 by more than 30 % (see Table I). Even with the smallest basis set ($n = 32 - 33$), the calculated binding energies exceed the experimental ones by more than 15 %. We conclude that a calculation based on the Fermi-pseudo potential [24] and the *ab-initio* calculated e -K scattering phase shifts can not yield consistent results for the set of states observed in this work. We thus explore a different approach, introducing an *ad-hoc* scaling of the 3S scattering length by 0.951 and choosing the closest-lying atomic Rydberg state as reference state (Eq. (1)). With these scattering parameters and a basis including only one asymptote below and above the state of interest, we reproduce all experimental binding energies for K₂ and CsK within the experimental uncertainty (see Appendix F). When following the same approach for Cs and setting Cs($31^2P_{3/2}$) (K($29^2P_{3/2}$)) as reference state in the calculations for Cs₂ (KCs), we have to reduce the 3S scattering length by about 13 % to match the experiment. A recent similar modelling of photoassociation resonances in rubidium has yielded a zero-energy 3S scattering length 5 % smaller than the most recent theoretical calculation [12, 31].

We conclude that (i) it seems necessary to set the

reference state to the closest-lying atomic state to obtain a consistent description of LRMs correlated to Rydberg states with different angular momentum l , (ii) for all three species, K, Cs, and Rb, the phase shifts extracted with help of the Fermi-pseudo potential model are significantly smaller than the ones obtained from high-level *ab-initio* calculations, and (iii) the extracted phase shifts depend on the basis set chosen for the calculation and should thus be considered effective, model-based parameters and not accurate determinations of the free-electron-atom scattering phase shifts. The set of experimental binding energies for the different homo- and heteronuclear LRMs presented here provides a challenge to the further development of theory, such as a possible extension of the Green's function formalism to include all relevant spin couplings. Assigning other

observed molecular resonances, which could originate from states located at shorter internuclear distances, will yield information about the energy dependence of the scattering phases. A full and accurate understanding of the PECs of heteronuclear LRMs is also prerequisite for schemes to probe spatial correlations in ultracold mixtures [25, 32] and to form strongly-coupled plasmas with variable mass ratios of oppositely charged particles [33].

We thank Frédéric Merkt for continuous and generous support, and Maximilian Beyer for extensive and helpful discussions. JD thanks Matthew Eiles, Chris Greene, and Ilya Fabrikant for helpful discussions. This work was supported by the ETH Research Grant ETH-22 15-1 and the NCCR QSIT of the Swiss National Science Foundation.

-
- [1] L. G. Marcassa and J. P. Shaffer, in *Adv. At. Mol. Opt. Phys.*, Vol. 63, edited by P. R. B. Ennio Arimondo and C. C. Lin (Academic Press, 2014) pp. 47–133.
 - [2] J. P. Shaffer, S. T. Rittenhouse, and H. R. Sadeghpour, *Nat. Commun.* **9**, 1 (2018).
 - [3] E. Fermi, *Il Nuovo Cimento* **11**, 157 (1934).
 - [4] C. H. Greene, A. S. Dickinson, and H. R. Sadeghpour, *Phys. Rev. Lett.* **85**, 2458 (2000).
 - [5] V. Bendkowsky, B. Butscher, J. Nipper, J. P. Shaffer, R. Löw, and T. Pfau, *Nature* **458**, 1005 (2009).
 - [6] J. Tallant, S. T. Rittenhouse, D. Booth, H. R. Sadeghpour, and J. P. Shaffer, *Phys. Rev. Lett.* **109**, 173202 (2012).
 - [7] M. A. Bellos, R. Carollo, J. Banerjee, E. E. Eyler, P. L. Gould, and W. C. Stwalley, *Phys. Rev. Lett.* **111**, 053001 (2013).
 - [8] D. A. Anderson, S. A. Miller, and G. Raithel, *Phys. Rev. Lett.* **112**, 163201 (2014).
 - [9] T. Niederprüm, O. Thomas, T. Manthey, T. M. Weber, and H. Ott, *Phys. Rev. Lett.* **115**, 013003 (2015).
 - [10] H. Saßmannshausen, F. Merkt, and J. Deiglmayr, *Phys. Rev. Lett.* **114**, 133201 (2015).
 - [11] B. J. DeSalvo, J. A. Aman, F. B. Dunning, T. C. Killian, H. R. Sadeghpour, S. Yoshida, and J. Burgdörfer, *Phys. Rev. A* **92**, 031403(R) (2015).
 - [12] F. Engel, T. Dieterle, F. Hummel, C. Fey, P. Schmelcher, R. Löw, T. Pfau, and F. Meinert, *Phys. Rev. Lett.* **123**, 073003 (2019).
 - [13] J. L. MacLennan, Y.-J. Chen, and G. Raithel, *Phys. Rev. A* **99**, 033407 (2019).
 - [14] H. Hotop, M. W. Ruf, and I. I. Fabrikant, *Phys. Scr.* **2004**, 22 (2004).
 - [15] J. M. Brown and A. Carrington, *Rotational Spectroscopy of Diatomic Molecules* (Cambridge University Press).
 - [16] J. Deiglmayr, H. Herburger, H. Saßmannshausen, P. Jansen, H. Schmutz, and F. Merkt, *Phys. Rev. A* **93**, 013424 (2016).
 - [17] M. Peper, F. Helmrich, J. Butscher, J. A. Agner, H. Schmutz, F. Merkt, and J. Deiglmayr, *Phys. Rev. A* **100**, 012501 (2019).
 - [18] H. Saßmannshausen, J. Deiglmayr, and F. Merkt, *Eur. Phys. J. Spec. Top.* **225**, 2891 (2016).
 - [19] M. Schlagmüller, T. C. Liebisch, F. Engel, K. S. Kleinbach, F. Böttcher, U. Hermann, K. M. Westphal, A. Gaj, R. Löw, S. Hofferberth, T. Pfau, J. Pérez-Ríos, and C. H. Greene, *Phys. Rev. X* **6**, 031020 (2016).
 - [20] K. M. Jones, E. Tiesinga, P. D. Lett, and P. S. Julienne, *Rev. Mod. Phys.* **78**, 483 (2006).
 - [21] W. Li, T. Pohl, J. M. Rost, S. T. Rittenhouse, H. R. Sadeghpour, J. Nipper, B. Butscher, J. B. Balewski, V. Bendkowsky, R. Löw, and T. Pfau, *Science* **334**, 1110 (2011).
 - [22] D. Booth, S. T. Rittenhouse, J. Yang, H. R. Sadeghpour, and J. P. Shaffer, *Science* **348**, 99 (2015).
 - [23] M. T. Eiles, *J. Phys. B: At., Mol. Opt. Phys.* **52**, 113001 (2019).
 - [24] M. T. Eiles and C. H. Greene, *Phys. Rev. A* **95**, 042515 (2017).
 - [25] M. T. Eiles, *Phys. Rev. A* **98**, 042706 (2018).
 - [26] A. A. Khuskivadze, M. I. Chibisov, and I. I. Fabrikant, *Phys. Rev. A* **66**, 042709 (2002).
 - [27] C. Fey, M. Kurz, P. Schmelcher, S. T. Rittenhouse, and H. R. Sadeghpour, *New J. Phys.* **17**, 055010 (2015).
 - [28] M. Dei, S. Haze, J. Wolf, L. Wang, F. Meinert, C. Fey, F. Hummel, P. Schmelcher, and J. Hecker Denschlag, *Phys. Rev. Research* **2**, 013047 (2020).
 - [29] E. Y. Sidky and I. Ben-Itzhak, *Phys. Rev. A* **60**, 3586 (1999).
 - [30] V. Bendkowsky, B. Butscher, J. Nipper, J. B. Balewski, J. P. Shaffer, R. Löw, T. Pfau, W. Li, J. Stanojevic, T. Pohl, and J. M. Rost, *Phys. Rev. Lett.* **105**, 163201 (2010).
 - [31] C. Bahrim, U. Thumm, and I. I. Fabrikant, *J. Phys. B: At., Mol. Opt. Phys.* **34**, L195 (2001).
 - [32] T. Manthey, T. Niederprüm, O. Thomas, and H. Ott, *New J. Phys.* **17**, 103024 (2015).
 - [33] M. Peper and J. Deiglmayr, *J. Phys. B: At., Mol. Opt. Phys.* **53**, 064001 (2020).
 - [34] B. R. Johnson, *J. Chem. Phys.* **69**, 4678 (1978).
 - [35] M. Beyer and F. Merkt, *Phys. Rev. Lett.* **116**, 093001 (2016).
 - [36] M. T. Eiles, *Highly Excited States of Small Molecules and Negative Atomic Ions*, Ph.D. thesis, Purdue University, West Lafayette (IN), United States of America (2018).

- [37] C. Bahrim, U. Thumm, and I. I. Fabrikant, Phys. Rev. A **63**, 042710 (2001).
- [38] P. Goy, J. M. Raimond, G. Vitrant, and S. Haroche, Phys. Rev. A **26**, 2733 (1982).
- [39] A. Omont, J. Phys. (Paris) **38**, 1343 (1977).
- [40] A. U. Hazi and H. S. Taylor, Phys. Rev. A **1**, 1109 (1970).
- [41] W. E. Milne, Phys. Rev. **35**, 863 (1930).
- [42] B. Yoo and C. H. Greene, Phys. Rev. A **34**, 1635 (1986).
- [43] E. P. Wigner, Phys. Rev. **98**, 145 (1955).
- [44] B. Butscher, V. Bendkowsky, J. Nipper, J. B. Balewski, L. Kukota, R. Löw, T. Pfau, W. Li, T. Pohl, and J. M. Rost, J. Phys. B: At., Mol. Opt. Phys. **44**, 184004 (2011).

A. DENSITY-DEPENDENT PHOTOASSOCIATION RATES OF HOMO- AND HETERONUCLEAR MOLECULES

The strengths of homo- and heteronuclear photoassociation resonances depend on the relative ground-state densities of the two species [25]. The strength of a photoassociation resonance of AB is proportional to

$$\mathcal{P}_{AB} = 4\pi V \rho_A \rho_B R_{e,AB}^2, \quad (2)$$

and the strength of a resonance of A_2 is proportional to

$$\mathcal{P}_{A_2} = 4\pi V \rho_A^2 R_{e,A_2}^2, \quad (3)$$

where $V\rho_A$ is the number of particles of species A in the effective photoassociation volume V and R_e is the equilibrium distance of the photoassociated molecule.

The relative strength of the photoassociation signal arising from heteronuclear AB molecules compared to A_2 molecules is thus optimized by maximizing the density ρ_B

while keeping the density ρ_A as small as possible. This density dependence is illustrated in Fig. I for $A = \text{Cs}$ and $B = \text{K}$. In the upper panel, the ratio ρ_K over ρ_{Cs} is 0.5, whereas in the lower panel the ratio is about 12. The PFI signals recorded for the two cases are remarkably different, with dominant features in the upper panel (dominant Cs density) at detunings of -37 MHz and -19 MHz . By comparison with the Cs_2^+ signal, these features can indeed be assigned to photoassociation of Cs_2 molecules. In contrast, the PFI signal in the lower panel (dominant K density) has a dominant feature at -27 MHz . This resonance can be assigned to the formation of CsK molecules because a similarly strong feature is absent in the PFI signal when the Cs density is dominant.

The different scaling of homo- and heteronuclear photoassociation rates is clearly visible in Fig. 1 of the main article. Here, the autoionization signals of CsK^+ and Cs_2^+ at isolated resonances far detuned from the transition from $\text{Cs}(6^2S_{1/2}(F=3))$ to $\text{Cs}(22^2P_{3/2})$ are shown for a series of experiments where the potassium density was kept constant at about $2.5(3) \cdot 10^{10} \text{ cm}^{-3}$ while the cesium density was varied. Panels a) and b) depict the spectra recorded for different densities whereas panel c) shows the total CsK^+ and Cs_2^+ ion yields derived from these spectra (integrated over frequency) as a function of the cesium density. As expected from Eqs. (2) and (3), the number of heteronuclear ions increases linearly with the cesium density, whereas the number of homonuclear ions depends quadratically on the cesium density. The respective scalings are highlighted by fitting the corresponding linear and quadratic models (Eq. (2) and (3)) to the data.

B. SCATTERING PHASE SHIFTS

For the calculation of e^- -Cs scattering phase shifts, we follow the procedure described by Khushkivadze *et al.* [26] using a model potential $V_{LS}(r)$ dependent on the angular momentum L and spin S of the e^- -Cs system. r is the electron-alkali-metal-atom distance.

The resulting coupled set of differential equations is solved numerically using the renormalized Numerov method [34] with a step size of $h = 5 \cdot 10^{-4} a_0$. At the end points of the integration, r_A and $r_{\text{end}} = r_A + h = 2000 a_0$, the wavefunction is matched to Riccati-Bessel functions [35]. The phase shifts obtained for the case of the e^- -Cs scattering with collision energies between 0 meV and 140 meV are depicted in Fig. II. Our results agree with the results reported in Ref. [26] within the resolution of their Figure 3.

The scattering phase shifts for the e^- -K collision have been calculated and reported by Eiles in Refs. [25, 36], Figure 1, from where we extract the phase shifts graphically. In his calculation, spin-orbit effects are neglected. From the 3P_0 - 3P_1 fine-structure splitting in Cs^- (3.78 meV) and its scaling with the nuclear charge Z and the principal quantum number n (4 for K and 6 for Cs)

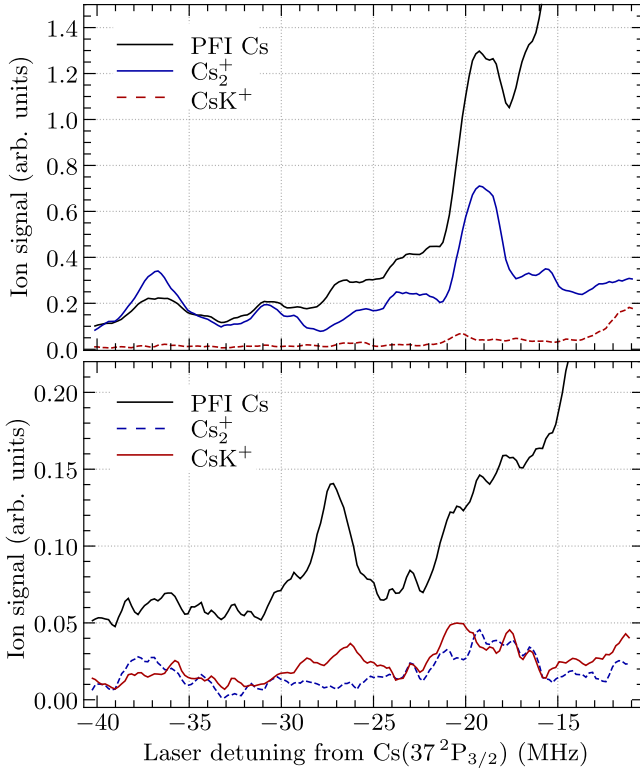


Figure I. Cs pulsed-field ionization (PFI) signal, Cs_2^+ , and CsK^+ ion signals as a function of the detuning of the photoassociation laser from the $\text{Cs}(37^2P_{3/2}) \leftarrow \text{Cs}(6^2S_{1/2}(F=3))$ transition. Prior to photoassociation, the K (Cs) atoms were prepared in the $F=1$ ($F=3$) hyperfine component of the ground state. For the spectra depicted in the upper panel, the Cs and K densities were set to $2.0 \cdot 10^{10} \text{ cm}^{-3}$ and $1.0 \cdot 10^{10} \text{ cm}^{-3}$, respectively. For the spectra depicted in the lower panel, the Cs and K densities were set to $0.4 \cdot 10^{10} \text{ cm}^{-3}$ and $4.7 \cdot 10^{10} \text{ cm}^{-3}$, respectively.

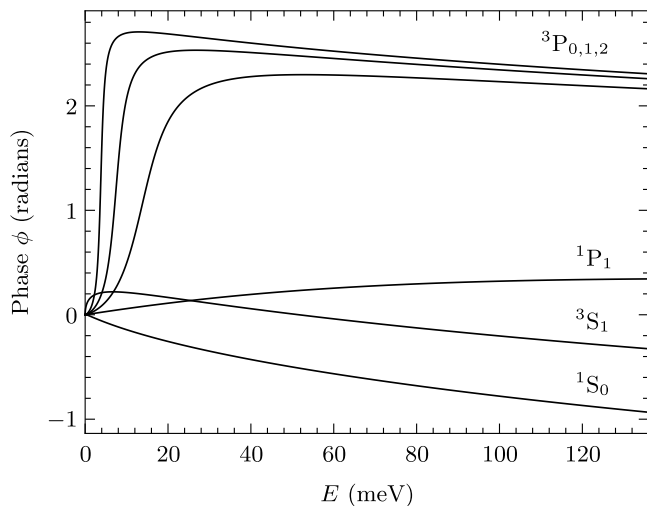


Figure II. Phase shifts of the e^- -Cs scattering process as a function of the electron kinetic energy E . The phase shifts for the electron collision with Cs are obtained by the method described in Ref. [26] including spin-orbit coupling.

as Z^4/n^3 [37], the 3P_0 - 3P_1 fine-structure splitting in K^- is estimated to be $182 \mu\text{eV}$. Neglecting the spin-orbit interaction in e^- -K scattering is therefore reasonable and hence we treat all three $^3P_{0,1,2}$ scattering phase shifts to be equal. Because the 3P_J shape resonance lies at much higher collision energies in e^- -K than in e^- -Cs collisions (24 meV vs 8 meV [25]), the resulting perturbations occur at shorter internuclear distances in K_2 than in Cs_2 .

C. CALCULATION OF INTERACTION POTENTIALS

We calculate the potential-energy curves (PEC) for homo- and heteronuclear long-range Rydberg molecules using the Hamiltonian given by Eiles and Greene [24]. This Hamiltonian explicitly includes the Fermi-contact interaction in a basis of good quantum numbers for the scattering problem β (scattering partial wave L , total electronic spin S , total angular momentum excluding nuclear spin J , and projection of J on the internuclear axis) in the pseudo-potential form

$$\hat{V}_{\text{FC}} = \sum_{\beta} |\beta\rangle \frac{(2L+1)^2}{2} a(SLJ, k) \frac{\delta(r)}{r^{2(L+1)}} \langle\beta|, \quad (4)$$

where the $a(SLJ, k)$ scattering parameters depend on the semi-classical wavevector k of the Rydberg electron at the position of the ground-state atom (see Eq. 1 in the main article), and r is the distance between Rydberg and ground-state atom. Via a frame-transformation matrix, the operator \hat{V}_{FC} is expressed in a basis of good quantum numbers ($nljm_j$) of the Rydberg atom, in which the operator \hat{V}_0 for the interaction of the Rydberg electron

with its core is diagonal with eigenvalues given by experimentally determined quantum defects [16, 17, 38]. The hyperfine interaction of the ground-state atom is included by the effective Hamiltonian

$$\hat{V}_{\text{HF}} = A_{\text{HF}} \vec{i} \cdot \vec{s}, \quad (5)$$

where A_{HF} is the hyperfine coupling constant and \vec{i} and \vec{s} represent the nuclear and electronic spin of the ground-state atom, respectively. We neglect the hyperfine interaction in the Rydberg atom, which scales as n^{-3} , and the interaction of the positively charged Rydberg core with the ground-state atom, because both contributions are typically too small to be observed at the resolution ($\sim 1.5 \text{ MHz}$) of our experiments.

The total Hamiltonian $\hat{H} = \hat{V}_0 + \hat{V}_{\text{HF}} + \hat{V}_{\text{FC}}$ is brought into matrix form in an atomic product basis, as described in the main article. It was shown that the pseudo-potential approach [24] with a basis set including two degenerate manifolds above and below the asymptote of interest reproduces the results of basis-set independent Greens function calculations [12, 27]. With this choice of basis, our calculations underestimate binding energies when K is the perturber and overestimate binding energies when Cs is the perturber and we thus treat the basis size as adjustable parameter of the calculation. Numerical diagonalization for different internuclear distances R yields the PECs. We have verified that our calculation reproduces the results (where potassium is the perturber) of Figures 3, 4, and 7 of Ref. [25] within the linewidth of the respective curves.

The projection of the total angular momentum excluding rotation on the internuclear axis Ω is a conserved quantity, and we perform the calculation separately for each Ω . The PECs for different values of Ω are in general degenerate. For P -wave contributions, this degeneracy is lifted by the spin-orbit interaction in the electron-neutral scattering state [28]. This effect is only important in heavy atoms, such as rubidium and cesium, and can be neglected for potassium. Fig. III and Fig. IV illustrate the effect of Ω on the PECs of selected states in Cs_2 and KCs , respectively, where Cs is the perturber. At the position of the outermost minimum around $R = 1400 a_0$, the interaction is dominated by S -wave interactions and the PECs for different values of Ω remain almost degenerate. Moving towards shorter internuclear distances, we encounter a minimum in the $^1,^3\Sigma^+$ PECs around $R = 1250 a_0$. Here the curves for different values of Ω have very different depths. We note that we have discussed these minima previously in the context of driving transitions to ion-pair states [33]. After solving the Schrödinger equation for the nuclear motion in the calculated Ω -dependent PECs (see next section), we find that the binding energy of the lowest level in the outermost well varies by less than 2 MHz (see wavefunctions and energies of the vibrational levels in Fig. III and Fig. IV) for $\Omega < 7/2$, and we thus report only the mean of these values.

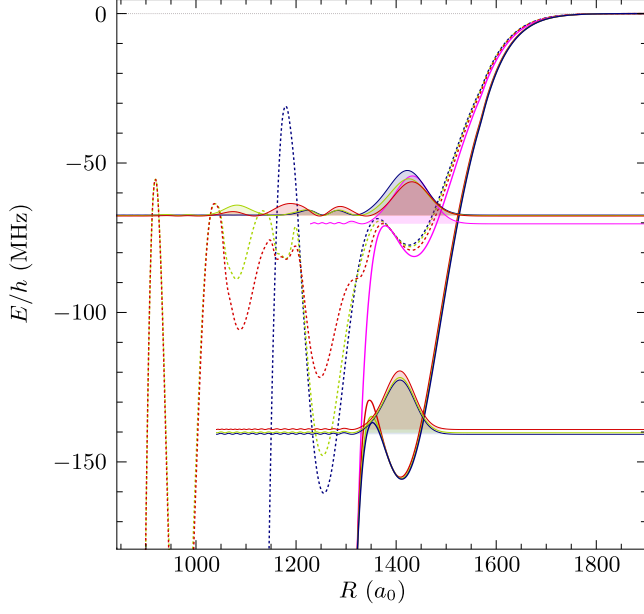


Figure III. $^3\Sigma^+(\Omega)$ (full) and $^1,^3\Sigma^+(\Omega)$ (dashed) interaction potentials correlating to the Cs($31^2P_{3/2}$)Cs($6^2S_{1/2}(F=3)$) asymptote with $\Omega = 1/2$ (blue), $\Omega = 3/2$ (green), $\Omega = 5/2$ (red), and $\Omega = 7/2$ (pink). The vibrational ground-states ($v=0$) in the outermost potential wells are given by full, filled lines.

We observe that the depth of the outermost well in the calculated PECs increases when (i) the basis set includes more hydrogenic manifolds above the state of interest and (ii) the reference state (Eq. 1 of the article) is changed from the higher-lying manifold to the low- l asymptote of interest. The latter can be understood as follows: the binding at an internuclear separation close to the outer turning point of the Rydberg electron is dominated by S -wave scattering. When the quantum defect of the reference state is reduced, the semi-classical kinetic energy of the e-atom scattering at a given distance also decreases (Eq. 1 of the article). Thus the value of the 1S and 3S scattering lengths decreases, *i.e.*, the absolute magnitude of the (negative) 3S scattering length increases and the well depth of the $^3\Sigma^+$ state increases. The binding of the mixed $^1,^3\Sigma^+$ state is dominated by the interaction in the 3S channel and thus also increases.

The calculations for CsK and K₂ presented in Figure 4 of the article show an interesting change of the phase of the oscillatory potential at $R \approx 1200 a_0$. This is caused by the transition from S -wave scattering ($\propto |\Psi(R)|^2$) to P -wave scattering ($\propto |\partial\Psi(R)/\partial R|^2$) as the semi-classical energy of the Rydberg electron at the position of the perturber increases (see Eq. 1 of the article) [39].

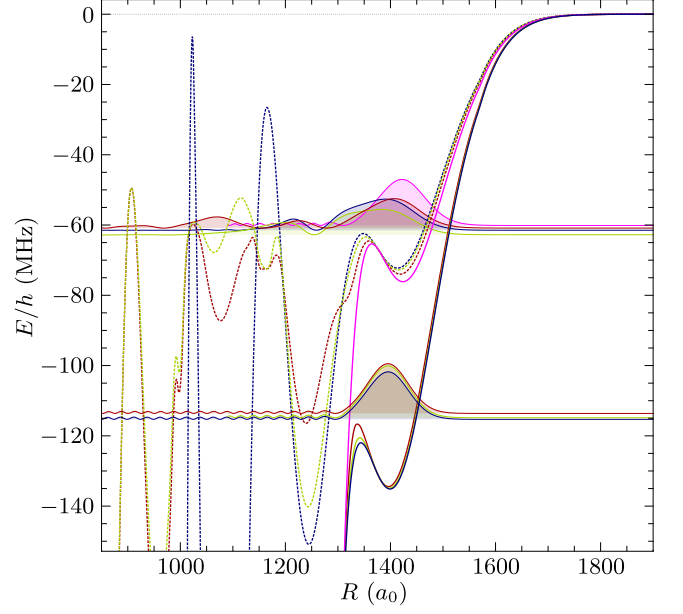


Figure IV. $^3\Sigma^+(\Omega)$ (full) and $^1,^3\Sigma^+(\Omega)$ (dashed) interaction potentials correlating to the K($29^2P_{3/2}$)Cs($6^2S_{1/2}(F=3)$) asymptote with $\Omega = 1/2$ (blue), $\Omega = 3/2$ (green), $\Omega = 5/2$ (red), and $\Omega = 7/2$ (pink). The vibrational ground-states ($v=0$) in the outermost potential wells are given by full, filled lines.

D. CALCULATION OF VIBRATIONAL WAVEFUNCTIONS

At small internuclear separations, the low-energy expansion of the Fermi-contact interaction breaks down, non-adiabatic couplings to other interaction potentials become important, and the behavior of the vibrational wavefunction is thus ill defined. Such a situation is, however, not uncommon in physics and several methods have been developed to overcome this problem, such as the stabilization method [40] and the Milne phase-amplitude method [29, 41]. For the calculation of vibrational wave functions, we adopt the modified Milne phase-amplitude method, as described by Sidky and Ben-Itzhak [29].

The central idea of the Milne method is that the wave function $\Psi_v(R)$ is replaced by the product of an R -dependent amplitude $\gamma(R)$ and the sine of an R -dependent phase $\phi(R)$

$$\Psi_v(R) = \sqrt{\frac{2\mu}{\pi}} \exp(\gamma(R)) \sin(\phi(R)) \quad (6)$$

in atomic units, with the reduced mass μ of the two-body problem. Making this substitution for the wavefunction in the Schrödinger equation of nuclear motion yields a set of differential equations

$$\frac{d^2\gamma}{dR^2} + \left(\frac{d\gamma}{dR}\right)^2 - \left(\frac{d\phi}{dR}\right)^2 + k^2(R) = 0, \quad (7)$$

$$\frac{d\phi}{dR} = \exp(-2\gamma). \quad (8)$$

The advantage of Eqs. (7) and (8) lies in the smooth behavior of the phase $\phi(R)$ and amplitude $\exp(\gamma(R))$ over the integration region, whereas $\Psi_v(R)$ is an oscillatory function. $\gamma(R)$ and $\phi(R)$ only remain smooth until the next maximum in the potential $V(R)$. Consequently the integration of Eqs. (7) and (8) is conducted in separate regions, as illustrated in Fig. V for the example of the $\text{Cs}(35^2\text{P}_{3/2})\text{Cs}(6^2\text{S}_{1/2}(F=4))\ ^3\Sigma^+(\Omega=1/2)$ interaction potential. The numerical integration in each region is started at the minimum of the potential region with the amplitude given by the WentzelKramersBrillouin (WKB) approximation [42] and the starting phase of the integration is chosen as $\phi = 0$. The wavefunction is then propagated to the next closest potential well, as indicated by the black arrows in the integration regions I to V indicated in the upper panel of Fig. V.

After the integration process, the solutions obtained for the separate integration regions are matched at the boundaries to obtain a continuous vibrational wave function $\Psi_v(R)$. This procedure relies on the fact that only the wavefunction $\Psi_v(R)$, and not the amplitude $\gamma(R)$ or phase $\phi(R)$, needs to be continuously differentiable. The phase in the outer classically forbidden region is kept at $\phi = 0$ and the amplitude at an inner end point of the integration (R_{in}) is kept at the value of the WKB approximation, ensuring energy normalization of the wave function. The resulting phase $\phi(R)$ and amplitude $\gamma(R)$ for a given energy E are plotted in the lower panel of Fig. V. The obtained wave function given by Eq. (6) is shown in red in the upper panel of Fig. V. For a calculation of bound vibrational states, the phase at the inner end point of the integration R_{in} is plotted against the energy E at which Eqs. (7) and (8) are solved, as shown in Fig. VI. When the energy of a bound vibrational state is reached, the phase jumps by π , as can be seen in the lower panel of Fig. VI. This property is an important advantage of the modified Milne phase-amplitude method over other methods such as the Numerov method, because the number of bound vibrational states in a certain region can be easily obtained by monitoring the respective phase shift and no bound states can be missed.

The spectrum of vibrational states can then be obtained from an energy derivative of the obtained phase $(\partial\phi(R_{\text{in}}, E)/\partial E)$, as shown in Fig. VI. The position and lifetime of vibrational bound states are obtained by fitting a Breit-Wigner line profile. The width of the resonance features corresponds to the strength of the coupling Γ_{cpl} to the short-range quasi-continuum. The Milne method does not only yield the eigenenergies and wavefunctions of vibrational levels, but also the characteristic time $\tau_{\text{cpl}} = 1/\Gamma_{\text{cpl}}$ for which the molecules stay localized in the outermost wells of the electronic state [43].

For example, for the resonance in the outermost potential well of the $\text{K}(29^2\text{P}_{3/2})\text{Cs}(6^2\text{S}_{1/2}(F=3))\ ^3\Sigma^+(\Omega=$

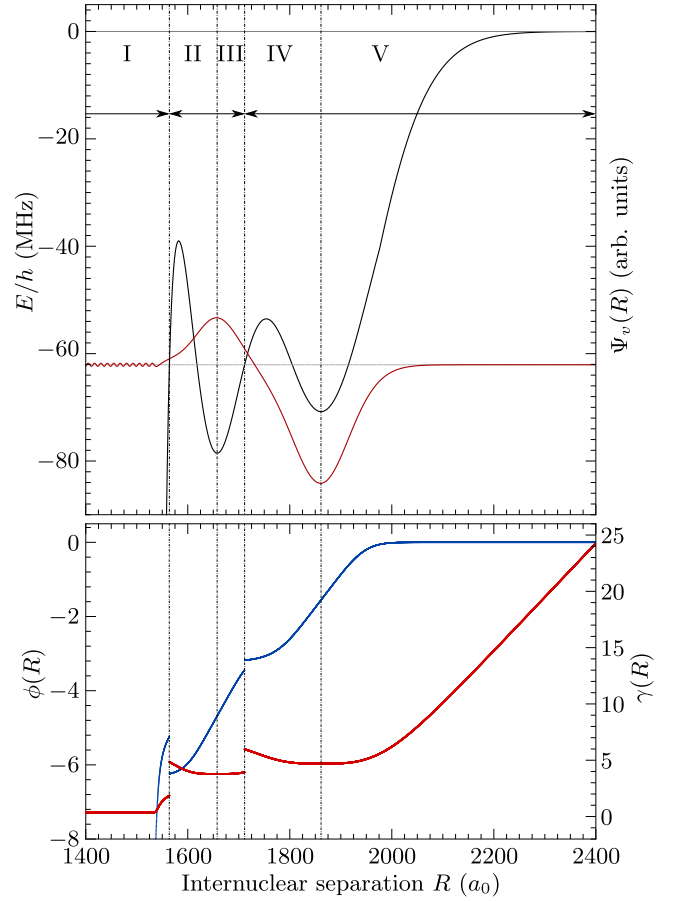


Figure V. (Upper panel) Vibrational wave function $\Psi_v(R)$ (red line) of a bound state in the $\text{Cs}(35^2\text{P}_j)\text{Cs}(6^2\text{S}_{1/2}(F=4))\ ^3\Sigma^+(\Omega=1/2)$ interaction potential. The integration was carried out separately in the region I to V in the directions indicated by the black arrows. (Lower panel) Obtained phase $\phi(R)$ (blue dots) and amplitude $\gamma(R)$ (red dots) after the matching procedure used to reconstruct the vibrational wave function Ψ_v (red line in the upper panel).

$1/2)$ electronic state, we determine a Breit-Wigner width of $\Gamma_{\text{FWHM}} = 7.9\text{ MHz}$ [43]. This is in good agreement with the experimental line width of $7.7(7)\text{ MHz}$. We interpret this width as natural linewidth of the resonance due to decay to shorter internuclear distances, where non-adiabatic transitions might cause a dissociation or autoionization of the long-range Rydberg molecule [44].

We note that in a harmonic potential, the zero-point energy scales as $1/\sqrt{\mu_{\text{AB}}}$ with the reduced mass μ_{AB} . The here calculated zero-point energies for the potentials with identical perturber follow this general trend, with significant deviations caused both by the anharmonicity of the PECs and the differences in the Born-Oppenheimer potentials.

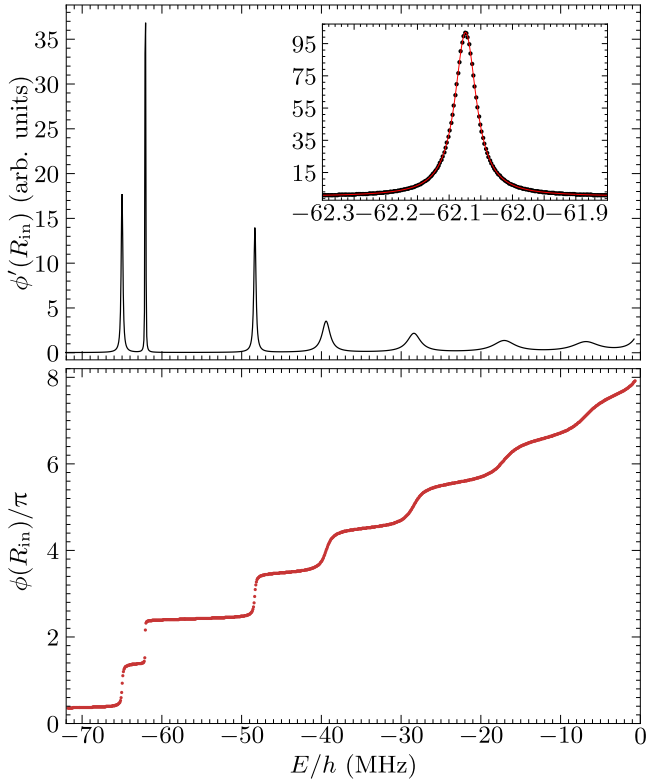


Figure VI. (Lower panel) Phase ϕ (red dots) of the wave function at an inner sampling point R_{in} at different energies E below the $\text{Cs}(35^2\text{P}_j)\text{Cs}(6^2\text{S}_{1/2}(F=4))$ in the interaction potential of the $^3\Sigma^+$ state. At the position of bound vibrational states, the value of the phase increases by π . (Upper panel) Energy derivative of the phase ϕ' giving the positions and widths of bound vibrational states. The inset shows the behavior around the most narrow feature close to -62.1 MHz calculated using a narrower energy grid. The lifetime of the bound state can be extracted from the width of the calculated resonance by a Lorentzian line fit (red line).

E. ASSIGNMENT OF PHOTOASSOCIATION RESONANCES

The interpretation of the recorded spectra depends crucially on a correct assignment of the observed resonances to vibronic levels of the LRM. In the K_2 autoionization spectrum recorded below the $\text{K}(29^2\text{P}_{3/2})\text{K}(4^2\text{S}_{1/2}(F=1))$ asymptote, the assignment is rather unambiguous and we identify the two strong resonances above -100 MHz as the $v=0$ levels of the $^3\Sigma^+$ and $^{1,3}\Sigma^+$ states, as indicated by the solid and dashed magenta lines. The CsK photoassociation spectrum recorded below the $\text{Cs}(31^2\text{P}_{3/2})\text{K}(4^2\text{S}_{1/2})$ asymptote is more congested. We assign the $v=0$ levels of the $^3\Sigma^+$ and $^{1,3}\Sigma^+$ states to the resonances marked by the solid and dashed green lines because their binding energies are close to the calculated value, and the Cs PFI signals are much stronger than the CsK autoionization signals, which is expected for the $v=0$

states in the outermost well (see Fig. 4 of the article). The $^3\Sigma^+$ resonance is accompanied by a second one at slightly larger detunings. For this more-strongly bound resonance, the relative yield of CsK^+ over Cs PFI ions is much larger than for the assigned resonance. We thus assume that this resonance originates from a state at shorter-range, which decays faster by autoionization. The resonances in the mm-wave spectrum below the $\text{Cs}(37^2\text{S}_{1/2})\text{K}(4^2\text{S}_{1/2}(F=2))$ asymptote are assigned based on the assignment and extrapolation of resonances at nearby asymptotes $\text{Cs}(n^2\text{S}_{1/2})\text{K}(4^2\text{S}_{1/2}(F=2))$ (see next section).

The assignment of the resonances in the KCs spectrum recorded below the $\text{K}(29^2\text{P}_{3/2})\text{Cs}(6^2\text{S}_{1/2}(F=3))$ asymptote is again rather unambiguous. In the Cs_2 spectrum recorded below the $\text{Cs}(31^2\text{P}_{3/2})\text{Cs}(6^2\text{S}_{1/2}(F=3))$ asymptote, the $^3\Sigma^+$ ($v=0$) resonance is easily identified. We assign the $^{1,3}\Sigma^+$ ($v=0$) resonance to the peak at larger detunings based on the calculated resonance structure.

F. MILLIMETER-WAVE SPECTROSCOPY

The lifetimes of long-range Rydberg molecules can exceed several microseconds, making it possible to perform millimeter-wave spectroscopy of these molecules. Millimeter-wave transitions allow one to probe molecular states which are inaccessible in a direct one-photon photoassociation such as molecular states lying below $n^2\text{S}_{1/2}$ asymptotes.

To this end, molecules are first formed by photoassociation with UV-laser pulses of typically $30\ \mu\text{s}$ length. Then pulses of millimeter-wave radiation are applied to the molecular sample with typical lengths of $10\ \mu\text{s}$. Subsequently, a ramped field-ionization pulse is applied and the Rydberg states are detected state-selectively. The state-selective detection of Rydberg molecules relies on the observation that the electronic wavefunction of low- l Rydberg molecules is dominated by the atomic character of the molecular dissociation asymptote. The molecules thus ionize at an electric field closely corresponding to the field at which the corresponding Rydberg atom would ionize. This property allows us to detect the transition from the vibrational ground state $v=0$ in the $^3\Sigma^+$ state associated with the $\text{Cs}(37^2\text{P}_{3/2})\text{K}(4^2\text{S}_{1/2})$ asymptote to molecules in states associated with the $\text{Cs}(n^2\text{S}_{1/2})\text{K}(4^2\text{S}_{1/2})$ asymptotes. Millimeter-wave spectra of $\text{Cs}(n^2\text{S}_{1/2})\text{K}(4^2\text{S}_{1/2}(F=2)) \leftarrow \text{Cs}(37^2\text{P}_{3/2})\text{K}(4^2\text{S}_{1/2}(F=2))$ transitions with $n=37, \dots, 40$ are depicted in Fig. VII. The upper panel depicts the $\text{Cs}(n^2\text{S}_{1/2})$ PFI and the lower panel depicts the CsK^+ ion signal as a function of the millimeter-wave frequency detuning from the respective atomic asymptote. The spectra show distinct peaks, both in the $\text{Cs}(n^2\text{S}_{1/2})$ PFI and the CsK^+ signals, indicating bound-millimeter-wave transitions. We assign these features on the basis of the Franck-Condon principle, which

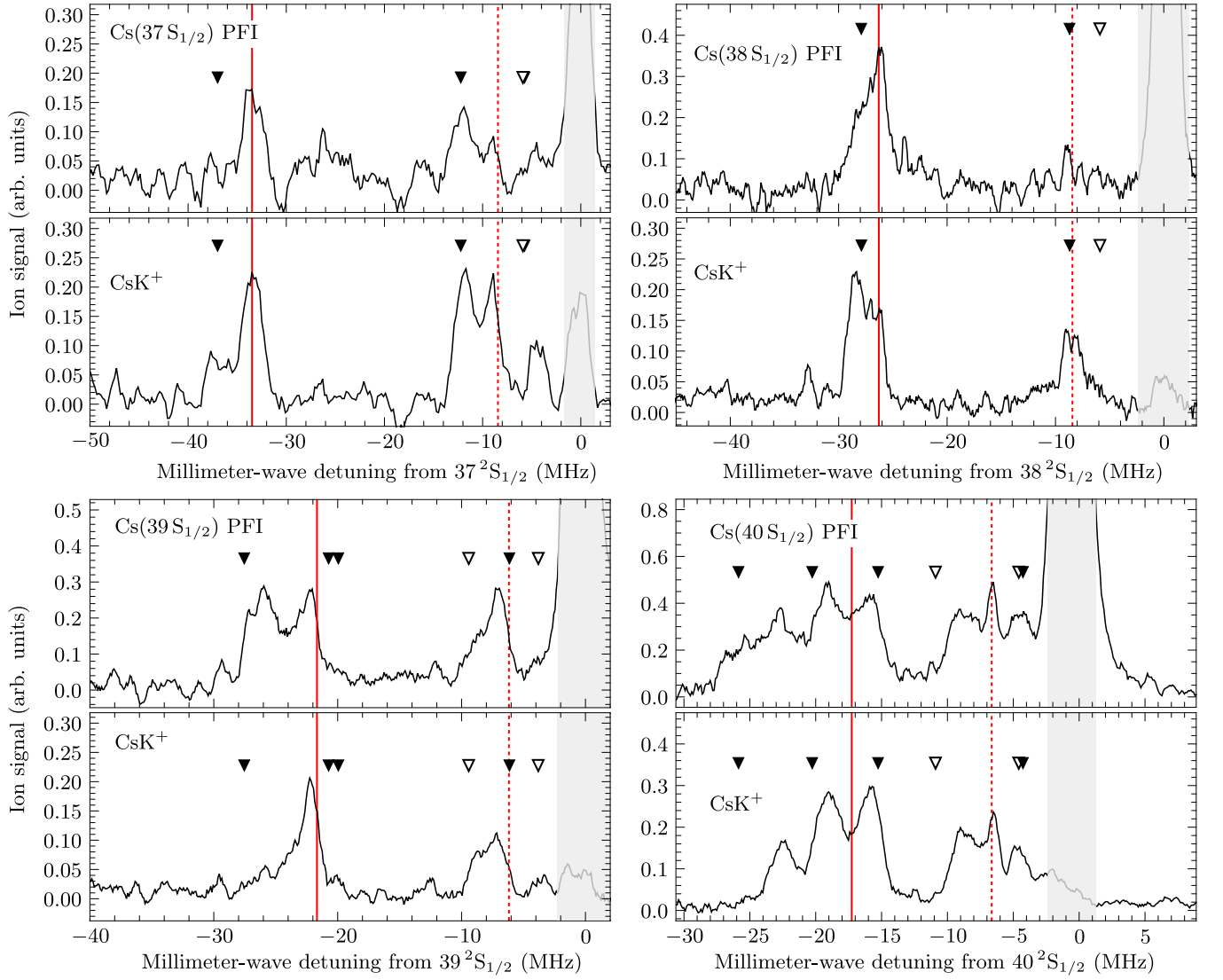


Figure VII. Millimeter-wave spectra of CsK molecules photoassociated in the vibrational ground state ($v = 0$) of the outermost potential well of the $\text{Cs}(37^2\text{P}_{3/2})\text{K}(4^2\text{S}_{1/2})\ ^3\Sigma^+$ interaction potential. The initial state was photoassociated by a $30\ \mu\text{s}$ UV laser pulse from a sample of Cs (K) atoms prepared in $F = 4$ ($F = 2$) hyperfine state. Using state-selective pulsed field ionization, the $n\text{S}_{1/2}$ and CsK^+ ion signal was recorded as a function of the millimeter-wave detuning from the (upper left) $\text{Cs}(37^2\text{S}_{1/2})\text{K}(4^2\text{S}_{1/2}(F = 2))$, (upper right) $\text{Cs}(38^2\text{S}_{1/2})\text{K}(4^2\text{S}_{1/2}(F = 2))$, (bottom left) $\text{Cs}(39^2\text{S}_{1/2})\text{K}(4^2\text{S}_{1/2}(F = 2))$, and (bottom right) $\text{Cs}(40^2\text{S}_{1/2})\text{K}(4^2\text{S}_{1/2}(F = 2))$ asymptotes. The calculated positions (see text for details) of the vibrational ground state in the outermost potential wells of the $^3\Sigma^+$ ($^1,^3\Sigma^+$) electronic state are indicated by full (dashed) red lines. The position of further bound states with overlapping initial and final vibrational wavefunctions are indicated by full (empty) triangles. Note that the calculations have been performed with *ad-hoc* scaled parameters.

allows only for transitions between states with overlapping vibrational wavefunctions of the final and initial molecular state.

For example, the molecular interaction potentials of the states involved in the $\text{Cs}(37^2\text{S}_{1/2})\text{K}(4^2\text{S}_{1/2}(F = 2)) \leftarrow \text{Cs}(37^2\text{P}_{3/2})\text{K}(4^2\text{S}_{1/2}(F = 2))$ transition are depicted in Fig. VIII. The $\text{Cs}(37^2\text{P}_{3/2})\text{K}(4^2\text{S}_{1/2}(F = 2))\ ^3\Sigma^+$ interaction potential of the initial level is shown in the upper panel in black and the position and probability density of the vibrational ground state in the

outermost potential well is given by a red filled line. The wavefunction of the initial state only has significant overlap with the outermost potential well of the $\text{Cs}(37^2\text{S}_{1/2})\text{K}(4^2\text{S}_{1/2}(F = 2))\ ^3\Sigma^+$ (green) and $^1,^3\Sigma^+$ (blue) interaction potential and therefore we assign the feature at $-33.4\ \text{MHz}$ in the $\text{Cs}(37^2\text{S}_{1/2})\text{K}(4^2\text{S}_{1/2}(F = 2)) \leftarrow \text{Cs}(37^2\text{P}_{3/2})\text{K}(4^2\text{S}_{1/2}(F = 2))$ millimeter-wave spectrum to a transition to the vibrational ground state of the $\text{Cs}(37^2\text{S}_{1/2})\text{K}(4^2\text{S}_{1/2}(F = 2))\ ^3\Sigma^+$ interaction potential.

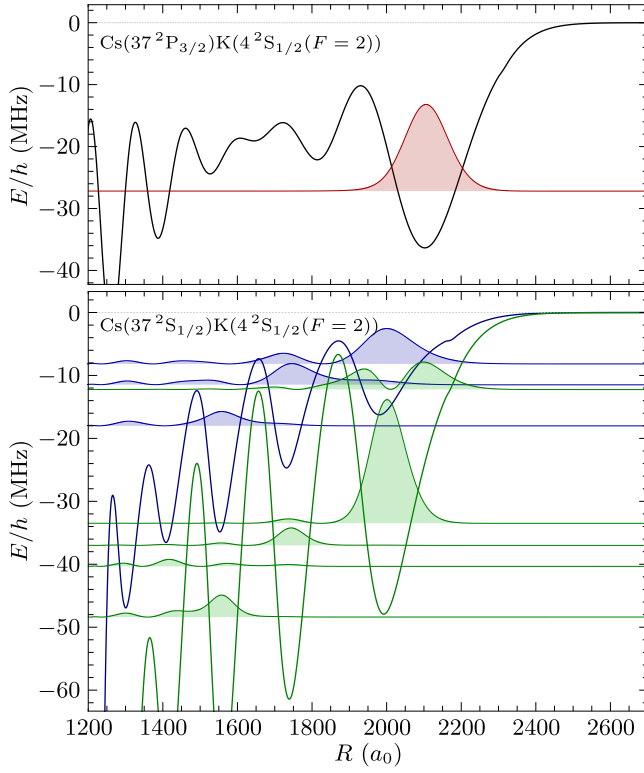


Figure VIII. (Upper panel) $^3\Sigma^+$ PEC (black) correlating to the $\text{Cs}(37^2\text{P}_{3/2})\text{K}(4^2\text{S}_{1/2}(F=2))$ asymptote. The energy and probability density of the vibrational ground state $v=0$ in the outermost potential is given by a red filled line. (Lower panel) Calculated PECs for $^3\Sigma^+$ (green) and $^{1,3}\Sigma^+$ (blue) states correlating to the $\text{Cs}(37^2\text{S}_{1/2})\text{K}(4^2\text{S}_{1/2}(F=2))$ asymptote. The energy and probability density of the vibrational levels in the respective potentials is given by green and blue filled lines. Note that the calculations have been performed with *ad-hoc* scaled parameters.

As mentioned in the main article, the basis set and scattering phase shifts used to reproduce the $\text{K}(29^2\text{P}_{3/2})\text{K}(4^2\text{S}_{1/2})$ and $\text{Cs}(31^2\text{P}_{3/2})\text{K}(4^2\text{S}_{1/2})$ binding energies systematically overestimate the binding energies of the vibrational ground states bound below the $\text{Cs}(n^2\text{S}_{1/2})\text{K}(4^2\text{S}_{1/2})2$ asymptotes. Therefore, we calculate the interaction potentials in a basis comprising the manifolds $n = (n_S - 5) \dots (n_S - 4)$ and scale the e-K ^3S scattering length by 0.951 to reproduce the experimental binding energy of the vibrational ground state of the $\text{Cs}(37^2\text{S}_{1/2})\text{K}(4^2\text{S}_{1/2}(F=2))$ $^3\Sigma^+$ interaction potential.

The resulting binding energies of the vibrational ground-states in the outermost potential well of the $^3\Sigma^+$ ($^{1,3}\Sigma^+$) interaction potential are depicted by red full (dashed) lines in Fig. VIII and summarized in Table II. The chosen scaling of the ^3S scattering length reproduces the position of features assigned to the $v=0$ level of the $^3\Sigma^+$ and the $^{1,3}\Sigma^+$ state for CsK molecules associated to $\text{Cs}(n^2\text{S}_{1/2})\text{K}(4^2\text{S}_{1/2})$, $\text{Cs}(31^2\text{P}_{3/2})\text{K}(4^2\text{S}_{1/2})$, and K_2 molecules associated to the $\text{K}(29^2\text{P}_{3/2})\text{K}(4^2\text{S}_{1/2})$

asymptote. Significant deviations are only observed for $\text{Cs}(n^2\text{S}_{1/2})\text{K}(4^2\text{S}_{1/2})$ with $n \geq 39$.

The millimeter-wave spectra become more congested with increasing n , because the overlap of the initial $\text{Cs}(37^2\text{P}_{3/2})\text{K}(4^2\text{S}_{1/2}(F=2))$ $^3\Sigma^+(v=0)$ bound state with other potential wells increases, as indicated in Fig. VIII. A similar effect can be observed for the $\text{Cs}(36^2\text{S}_{1/2})\text{K}(4^2\text{S}_{1/2}) \leftarrow \text{Cs}(34^2\text{P}_{3/2})\text{K}(4^2\text{S}_{1/2})$ millimeter-wave transition. The spectra recorded with the potassium ground-state atom prepared in the $F=1$ and $F=2$ hyperfine state are presented in Fig. IX. In order to remove noise caused by fluctuations in the number of photoassociated molecules from millimeter-wave spectra, we consider the ratio $Q_{36\text{S}}(Q_{\text{CsK}})$ of the signal detected in the integration window of the $36^2\text{S}_{1/2}$ PFI (CsK^+) signal over the PFI ion signal of the initial state.

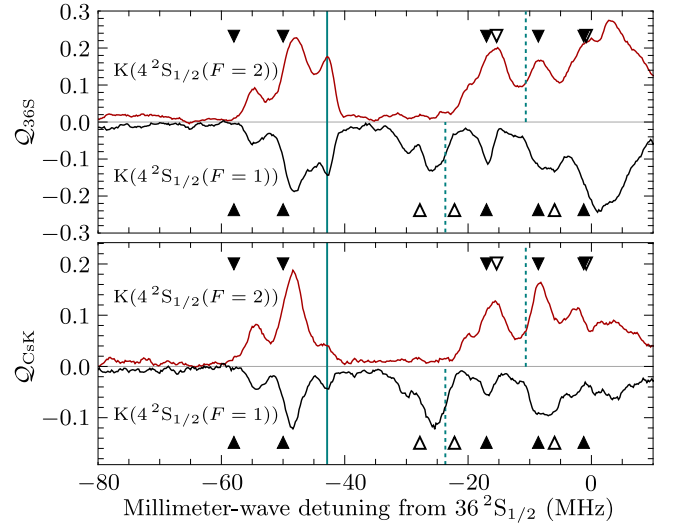


Figure IX. Millimeter-wave spectra of CsK molecules photoassociated in the vibrational ground state of the outermost potential well of the $\text{Cs}(34^2\text{P}_{3/2})\text{K}(4^2\text{S}_{1/2})$ $^3\Sigma^+$ state by a $30\mu\text{s}$ UV laser pulse. Before photoassociation, the ^{39}K atoms were prepared either in the $F=1$ (black) or $F=2$ (red) hyperfine component of the ground-state atom. The upper panel depicts the ratio $Q_{36\text{S}}$ of transferred Rydberg atoms and the lower panel depicts the ratio Q_{CsK} after a millimeter-wave pulse of $10\mu\text{s}$ length with a frequency close to the $\text{Cs}(36^2\text{S}_{1/2}) \leftarrow \text{Cs}(34^2\text{P}_{3/2})$ transition. The horizontal scale gives the detuning from the dissociation asymptote $\text{Cs}(36^2\text{S}_{1/2})\text{K}(4^2\text{S}_{1/2})$ and thus corresponds to the binding energy of the final molecular states. For clarity, the sign of the black trace is inverted and constant offsets of 0.12 and 0.13 (arb. units) were subtracted from $Q_{36\text{S}}$ and Q_{CsK} , respectively. The calculated positions (see text for details) of the $v=0$ level in the outermost potential well of the $^3\Sigma^+$ ($^{1,3}\Sigma^+$) electronic state are indicated by full (dashed) cyan lines. The position of further vibrationally bound states with overlapping vibrational wavefunctions of the initial and final molecular state are indicated by full and empty triangles for $^3\Sigma^+$ and $^{1,3}\Sigma^+$, respectively. Note that the calculations have been performed with *ad-hoc* scaled parameters.

Table II. Calculated (D_0) and experimental ($D_{0,\text{exp}}$) binding energies of the $v = 0$ level of the outermost well using the *ad-hoc* scaled 3S scattering length. The experimental uncertainty is estimated from the calibration uncertainty (see text) and the linewidth.

Asymptote	State	D_0/h (MHz)	$D_{0,\text{exp}}/h$ (MHz)
Cs($36\ ^2S_{1/2}$)K($4\ ^2S_{1/2}(F)$)	$^3\Sigma^+$	-42.9	-43.0(5)
	$^{1,3}\Sigma^+(F=1)$	-23.7	-25.7(5)
	$^{1,3}\Sigma^+(F=2)$	-10.5	—
Cs($37\ ^2S_{1/2}$)K($4\ ^2S_{1/2}(F)$)	$^3\Sigma^+$	-33.5	-33.4(5)
	$^{1,3}\Sigma^+(F=2)$	-8.2	-9.1(5)
Cs($38\ ^2S_{1/2}$)K($4\ ^2S_{1/2}(F)$)	$^3\Sigma^+$	-26.3	-26.4(5)
	$^{1,3}\Sigma^+(F=2)$	-8.4	-8.4(5)
Cs($39\ ^2S_{1/2}$)K($4\ ^2S_{1/2}(F)$)	$^3\Sigma^+$	-21.7	-22.2(5)
	$^{1,3}\Sigma^+(F=2)$	-6.2	-7.2(5)
Cs($40\ ^2S_{1/2}$)K($4\ ^2S_{1/2}(F)$)	$^3\Sigma^+$	-17.3	-19.1(5)
	$^{1,3}\Sigma^+(F=2)$	-6.6	—
Cs($31\ ^2P_{3/2}$)K($4\ ^2S_{1/2}(F)$)	$^3\Sigma^+$	-83.9	-82.7(15)
	$^{1,3}\Sigma^+(F=1)$	-47.5	-47.8(15)
K($29\ ^2P_{3/2}$)K($4\ ^2S_{1/2}(F)$)	$^3\Sigma^+$	-74.9	-74.5(20)
	$^{1,3}\Sigma^+(F=1)$	-40.9	-42.1(20)

The spectra reveal several transitions to vibrational bound states including a triplet between -55 MHz and -40 MHz, which by comparison of the spectra recorded with the potassium ground-state atoms prepared in the $F = 1$ and $F = 2$ state can be assigned to states bound

in the $^3\Sigma^+$ state. By comparison with calculations, this triplet can be assigned to transitions to the vibrational ground states $v = 0$ of the three outermost potential wells as depicted in Fig. VIII for the state correlated to Cs($37\ ^2S_{1/2}$)K($4\ ^2S_{1/2}$).